



# Design, fabrication, and measurement of a miniaturized MIMO antenna applicable for 5G communication

Ankan Bhattacharya

Department of Electronics and Communications Engineering, Hooghly Engineering & Technology College, Hooghly, West Bengal, India

## Research Paper

**Cite this article:** Bhattacharya A (2024) Design, fabrication, and measurement of a miniaturized MIMO antenna applicable for 5G communication. *International Journal of Microwave and Wireless Technologies* 16(4), 567–578. <https://doi.org/10.1017/S1759078724000096>

Received: 1 June 2023  
Revised: 24 December 2023  
Accepted: 5 January 2024

**Keywords:**  
5G communication; bandwidth;  
enhanced isolation; MIMO antenna

Email: [bhattacharya.ankan1987@gmail.com](mailto:bhattacharya.ankan1987@gmail.com)

### Abstract

The design of low-profile Multiple-Input-Multiple-Output (MIMO) antennas for various 5G applications is a topic of huge interest in academia, research, and telecommunication sector. In this aspect, a compact and low-profile 5G MIMO antenna has been designed and analyzed for various 5G applications, specifically for the 24 GHz bands (24.25–24.45 GHz and 25.05–25.25 GHz) and local multipoint distribution system band (27.5–28.35 GHz) of the 5G spectrum. The proposed antenna structure is  $20 \times 20 \times 1$  mm<sup>3</sup> in dimension. Two spade-shaped radiators composed of Copper (annealed) material are placed orthogonally to improve isolation and maintain signal diversity. Rogers RT 5880 is used as the material for substrate. The antenna exhibits a wide bandwidth of 21.5–28.5 GHz. The mutual isolation  $|S_{21}|$  has been maintained  $\leq 29$  dB due to the insertion of a T-shaped parasitic strip in between the radiating elements. Novelty in design and superiority in performance has been observed when compared with related antenna categories.

### Introduction

The landscape of contemporary wireless technology has been dramatically altered by 5G. It is becoming incredibly well-liked in the fields of academia, research, and telecommunications. The International Telecommunications Union (ITU) has considered a number of millimeter wave spectrums for 5G communication in order to get around the bandwidth restrictions of 4G communications, including the 24/25 GHz bands covering 24.25–24.45 GHz and 25.05–25.25 GHz, the 27/29 GHz bands covering 27.5–28.35 GHz and 29.1–29.25 GHz, the 31 GHz band covering 31.0–31.3 GHz, the 42 GHz band stretching from 42.0 to 42.5 GHz, the 39/40 GHz band spanning 38.6–40.0 GHz, the 37/38 GHz bands spanning 37.0–38.6 GHz, and a few other higher frequency bands [1]. Few innovative MIMO structures have been studied by renowned antenna experts worldwide to perceive high data transfer rates. High bandwidth, gain, and data rate are fundamental needs for 5G communications, which are provided by antenna arrays in MIMO mode [2–5]. For phased array systems, a number of antenna types, including angled dipoles and Yagi-Uda like characteristics, are proposed in [6, 7]. In [8], a brand-new dipole antenna that is balun-fed is demonstrated. A structure for an inverted F-shaped antenna array has been given in [9]. For 5G-specific applications, a cavity-backed, dual-polarized array antenna has been proposed in [10, 11], which supports the use of a tapered, slotted antenna that is miniature. A 3D phased array antenna with a planar shape has been suggested in [12]. In [13], a rectangular dielectric resonator antenna with a changed feed was studied. In [14], a high-gain antenna element based on stacked/layered patches was suggested [15], which presents a co-planar waveguide-fed antenna with a partial ground plane. In [16], a wideband antenna with integrated Low Pass Filter (LPF) and slotted ground and feeding ports in the top layer has been provided. The radiating elements in tiny MIMO antennas or array structures are positioned close together. This proximity creates the issue of mutual coupling and lowers the level of isolation [17–22]. Many strategies have been used to reduce the impact of mutual coupling, including metal covers, bended strips, slotted isolators, frequency selective structures, rectangular slots, self-diplexing techniques, and crosslines [23–25]. The size and design of these planned MIMO antenna arrays continue to be a problem, though. Mutual coupling has a clear negative influence on the isolation level of a MIMO antenna.

Therefore, it is a challenge for all antenna researchers to develop a compact construction and include cutting-edge methods that might lessen the coupling effect. In this work, we have looked into a small, printed, two-element array antenna that is configured for MIMO. To achieve variation in the radiation pattern, two metallic spade-shaped radiators have been placed orthogonally above the substrate. We added a T-shaped parasitic element between the radiators to increase isolation. The operating bandwidth is increased by the introduction of rhombic slots in

**Table 1.** Comparison table of prominent 5G MIMO antennas in terms of size and performance

Ref.	Technique used	Size (in terms of $\lambda$ , where $\lambda$ denotes free space wavelength), mm <sup>3</sup>	Substrate material	Dielectric constant	Loss tan. ( $\tan \delta$ )	Bandwidth, GHz	Gain (avg.), dBi	Magnitude of TARC	Rad. Eff. (avg.)	Isolation $ S_{21} $ , dB
[9]	Planar inverted-F antenna with anti-resonating structure	50 × 100 × 3.5	Taconic TLC	3.2	3.2	2–3.6	10.08	NA	NA	≤20
[10]	Dual-polarized, cavity-backed antenna array	140 × 140 × 13	Rogers RT 5880	2.2	0.0004	4.9–6	9.05	≤7 dB	80%	≤20
[11]	Miniaturized tapered slot antenna	82.0 × 50.0 × 0.8	Rogers RT 5880	2.2	0.0004	21.0–23.0	12.03	NA	90%	≤12
[12]	Planar switchable 3D-coverage phased array	65 × 130 × 0.764	Nelco N9000	3.0	0.005	27–29	8.0	NA	80%	≤10
[13]	Rectangular Dielectric Resonator Antenna with modified feed	50 × 40 × 0.254	RT/Duroid 5880	2.2	0.0004	27–29.1	9.76	NA	NA	≤15
[14]	High-gain antenna elements, based on stacked patches	32.1 × 37.45 × 2.124	Rogers 5880	2.2	0.0004	23–32	11 dBi	≤7 dB	NA	≤17.5
[15]	Co-planar waveguide fed radiating patch with split resonators and partial ground	50.8 × 12 × 0.8	RT Duroid 5880	2.2	0.0004	25.1–37.5	7.7 dBi	NA	80%	≤22
[16]	Slotted ground and microstrip feeding ports in the top layer with integrated LPF	77.8 × 158 × 0.381	RT/duroid–5880	2.2	0.0004	27.5–40	7.2	≤5 dB	75%	≤17
[17]	CSRR-loaded CPW-fed antenna	25 × 25 × 1.6	FR4	4.4	0.025	5.28–5.52/6–7.2	2.54	NA	89%	≤20
[18]	Koch Fractal printed MIMO	26 × 35 × 1.5	AR600	6	0.0022	2.0–10.6	3.5	NA	NA	≤ 22
[19]	Four-port UWB MIMO with meandered slots	40 × 40 × 0.8	FR4	4.4	0.025	2.54–10.74	NA	NA	NA	≤15
This work	Orthogonal radiators with T-shaped decoupling element and CPW	20.0 × 20.0 × 1	RT/duroid–5880	2.2	0.0004	21.5–28.5	8.1	≤–10 dB	81%	≤29

TLC: Thomson Lamination Company, CSRR: Complementary split ring resonator, UWB: Ultra Wideband.

ground plane. A broad bandwidth of 21.5–28.5 GHz was demonstrated by the final antenna structure. The measured isolation level  $|S_{21}|$  is 29 dB, which is unquestionably a significant advancement for improving isolation of tiny MIMO antenna structures. On the basis of design and performance, Table 1 compares prominent MIMO antennas made for various 5G applications.

### Antenna design and simulation

Our objective is to design a wideband MIMO antenna. The process started with designing of a single-antenna element, and after successive iterations, the structure of the single element antenna has been finalized. The successive design stages of the single-antenna element with their frequency responses have been depicted in Fig. 1.

Design-I consists of a simple rectangular-shaped patch. The shape and size of the rectangular patch have been modified in Design II. The advantages of spade-shaped patches have been studied in [26–28]. The goal of radiating structures with spade shapes is to aid in the development of several resonant frequencies, which later combine to form a wide frequency band. So, with the

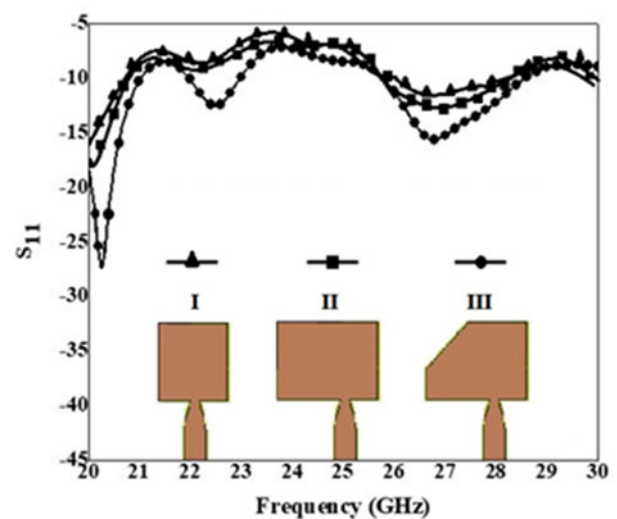


**Figure 1.** Successive design stages and responses of single-antenna element.

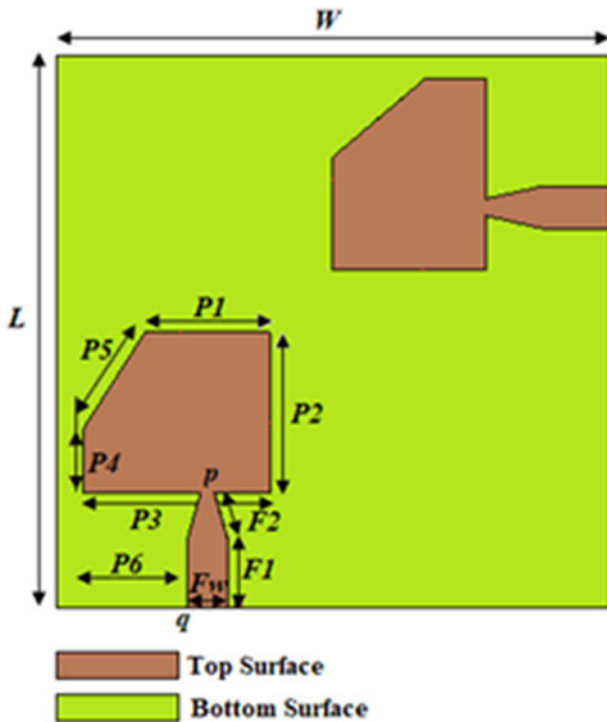


Figure 2. MIMO antenna with orthogonal spade-shaped radiators (Antenna I).

aim of increasing the bandwidth, the patch is given the shape of a spade in Design III, which exhibits better response in comparison with the former designs (Fig. 1).

A MIMO antenna structure has many advantageous features such as higher data rate, time diversity, frequency diversity, reduced signal distortion, and higher accuracy. Common MIMO configurations are  $2 \times 2$ ,  $3 \times 3$ ,  $4 \times 4$ ,  $8 \times 8$  etc. In order to maintain the design simplicity and uniformity and space conservation and enhanced isolation between antenna elements, a  $2 \times 2$  MIMO antenna structure has been proposed here.

The process started with the blueprint for Antenna I (Fig. 2), which consists of two spade-shaped radiators constructed of copper that have been annealed and mounted on top of an RT/Duroid substrate with a dielectric constant of 4.4 and a loss tangent of 0.0004.

The radiators are kept orthogonal to improve the mutual isolation and to maintain the diversity in signal transmission/reception. A continuous ground plane made of copper material exists

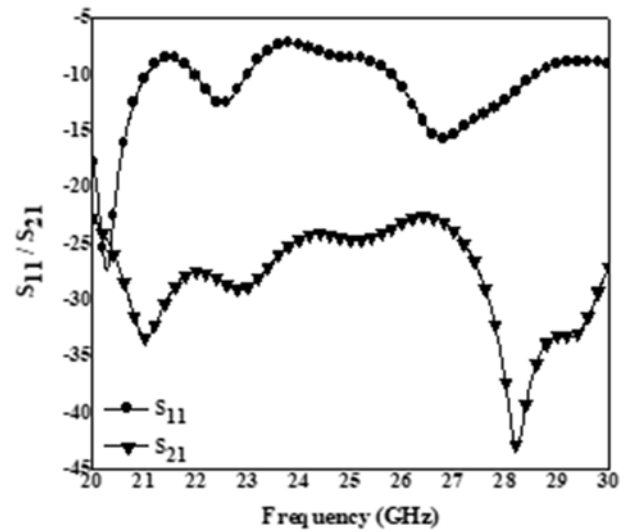


Figure 3. S-parameter vs. frequency response of Antenna I.

beneath the 1.0 mm thick substrate. Two orthogonally organized microstrip lines that are matched to a load impedance of 50  $\Omega$  for exciting the radiators. Using altered geometrical structures as radiating elements, it is possible to increase the impedance bandwidth and add new resonant frequencies, as described in [29]. After a certain number of simulation rounds, each radiating element has been adjusted to produce the most optimized response. The offset-feeding methodology suggested here offers a significantly larger impedance spectrum when compared to the traditional center feeding method [30]. The benefits of aligning the radiating elements perpendicularly include better isolation and polarization variability. The planar construction has the following dimensions:  $20 \times 20 \times 1 \text{ mm}^3$ . The structure demonstrated a multiband frequency response covering three distinct frequency bands 20–21.5 GHz, 22–23 GHz, and 26–29 GHz after simulation in CST Microwave Studio Suite<sup>TM</sup>. In this instance, the isolation level obtained is  $-24 \text{ dB}$  (Fig. 3).

It should be observed that at 20.3, 22.5, and 27 GHz, respectively, there are essentially three resonant modes. Figure 4 depicts the antenna surface current flow in Antenna I for three distinct resonating frequencies. Figure 5 shows the field magnitude at appropriate frequency points.

Deformation or a flaw in the antenna ground plane is a very effective technique that may be used to enhance frequency responsiveness. Defective ground structures aid in bandwidth control,

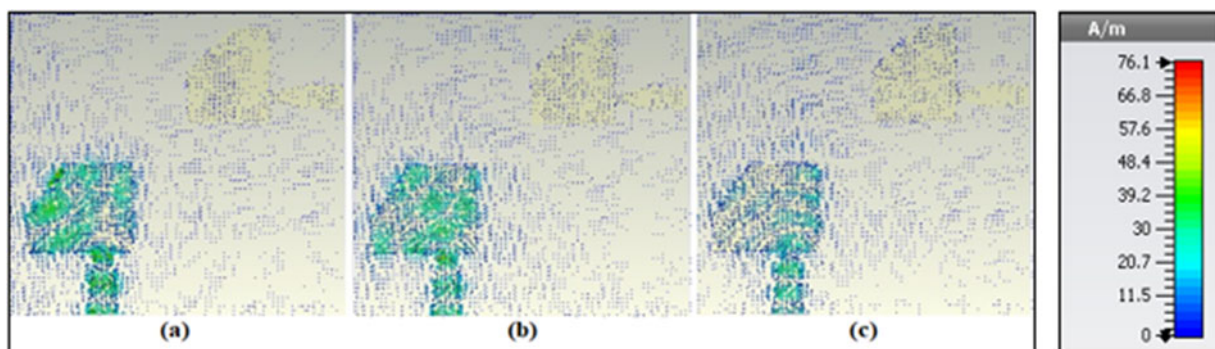


Figure 4. Pattern of surface current flow of Antenna I with Port 1 in excited mode at: (a) 20.3 GHz, (b) 22.5 GHz, (c) 27 GHz.

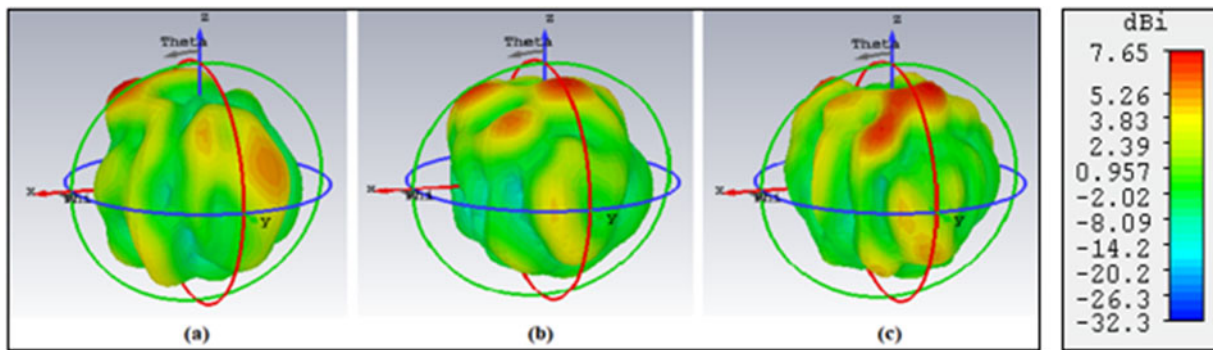


Figure 5. Far-field magnitude of Antenna I at: (a) 20.3 GHz, (b) 22.5 GHz, and (c) 27 GHz.

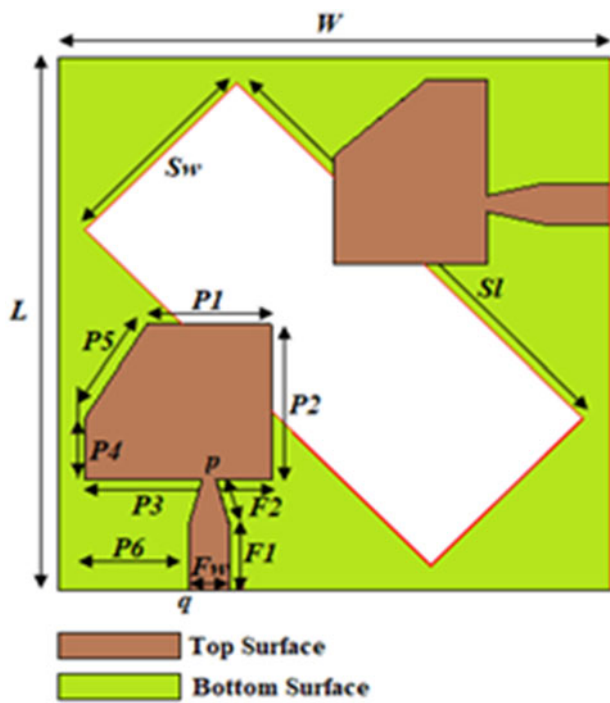


Figure 6. MIMO antenna with orthogonal spade-shaped radiators and rhombic slot in the ground plane (Antenna II).

impedance matching, and surface-wave suppression [31]. A slotted structure in the shape of a rhombus produces a wide bandwidth, offers low tolerance for mass alignment, and is also simpler to fabricate or print. The installation of the rhombic slot in the ground plane, which is responsible for the formation of new resonant modes, can be shown to have increased the magnetic field's strength as well as the E-field's magnitude. The ground of Antenna I has a rhombic-shaped slot cutout of it with the goal of increasing bandwidth even more. Antenna II is the newly formed structure (Fig. 6). The dimensions of the rhombic slot have been chosen by fine tuning the slot dimensions namely slot width,  $S_w$ , and slot length,  $S_l$ . The best response is obtained when the slot dimensions are kept as  $S_w = 7.0$  mm and  $S_l = 16.0$  mm. The change of antenna frequency response with respect to variation in antenna parameters  $S_w$  and  $S_l$  has been depicted in Fig. 7.

In simulation, Antenna II displayed a wide bandwidth, spanning 20–28 GHz, and a little improvement in isolation level of  $|S_{21}| = 25$  dB (Fig. 8). It is evident that there is a deviation in the

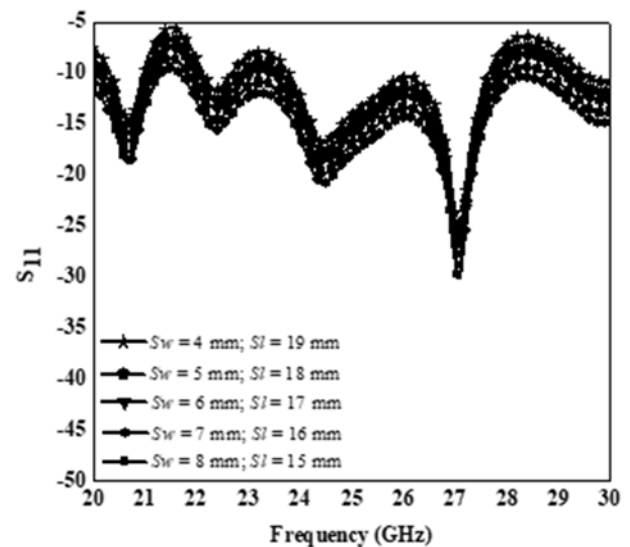


Figure 7. Change in antenna frequency response due to variation of  $S_w$  and  $S_l$ .

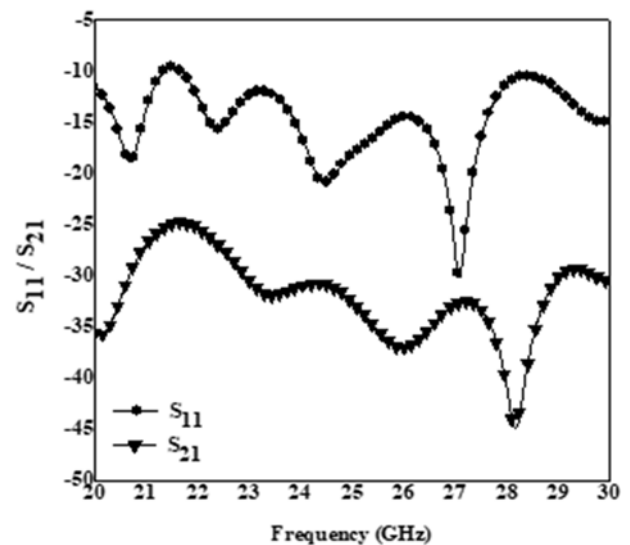


Figure 8. S-parameter vs. frequency response of Antenna II.

flow of antenna current along the ground plane as a result of the presence of the rhombic slot.

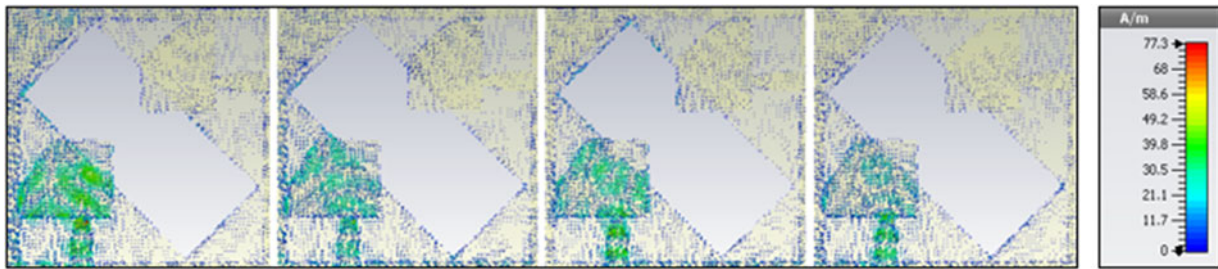


Figure 9. Pattern of surface current flow of Antenna II with Port 1 in excited mode at: (a) 20.9 GHz, (b) 22.1 GHz, (c) 24.5 GHz, d) 27 GHz.

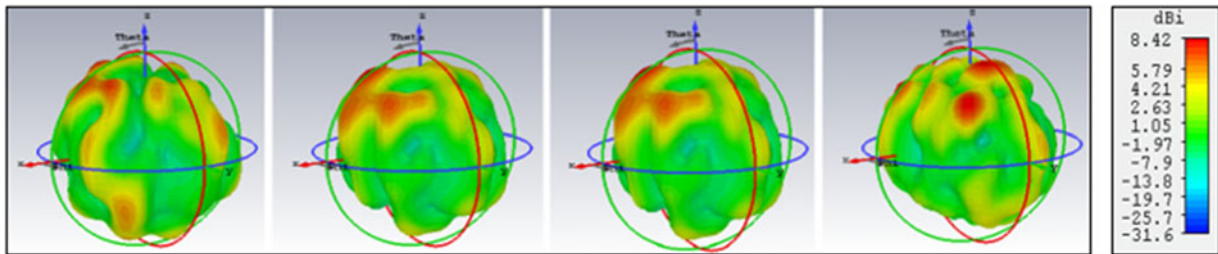


Figure 10. Far-field magnitude of Antenna II at: (a) 20.9 GHz, (b) 22.1 GHz, (c) 24.5 GHz, and (d) 27 GHz.

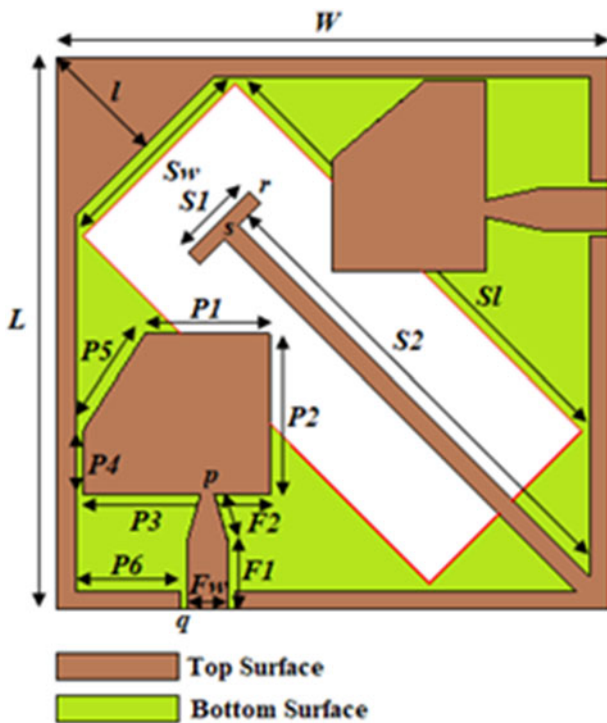


Figure 11. MIMO antenna with orthogonal spade-shaped radiators, rhombic slot in the ground plane and T-shaped parasitic element (Antenna III).

It is clear that the addition of a ground plane slot has caused a deviation in the flow of antenna surface current, increasing the average magnetic field intensity and, consequently, expanding the impedance bandwidth. Figure 9 shows the surface current flow pattern of Antenna II with Port 1 activated at the resonance frequencies of 20.8 GHz, 22.2 GHz, 24.3 GHz, and 27 GHz. The field magnitude of Antenna II at the same frequency points is depicted in Fig. 10.

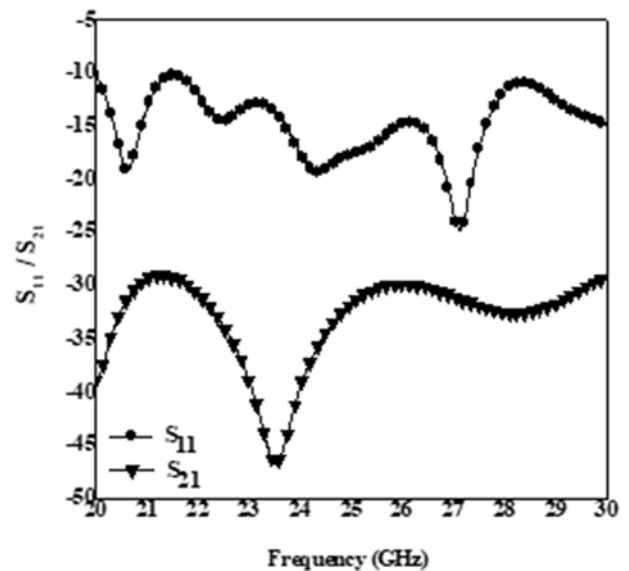
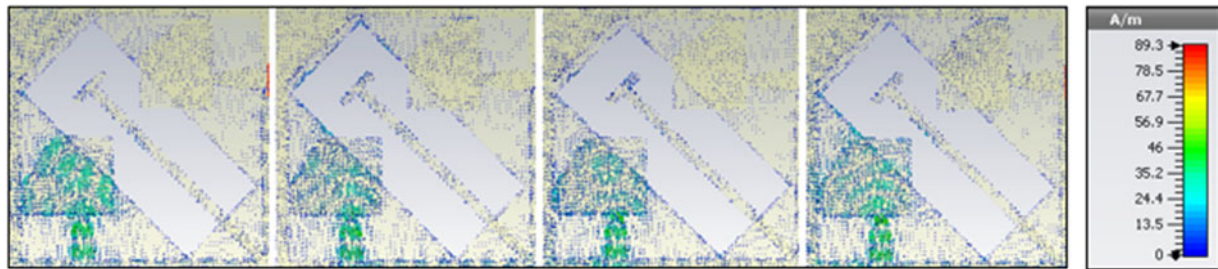


Figure 12. S-parameter vs frequency response of Antenna III.

The single-antenna element provides multiband response. A MIMO structure has been incorporated to introduce the advantageous features of the same such as higher data rate, time diversity, frequency diversity, reduced signal distortion, and higher accuracy. In order to maintain the design simplicity and uniformity and space conservation and enhanced isolation between antenna elements, two radiating structures, placed orthogonally have been placed.

There has been a negligible change in the frequency response of Antenna I due to the insertion of the second element. However, there has been an abrupt change in the response when there is a deformation in the ground plane. The reason for the same can be explained with the aid of antenna surface current distribution.



**Figure 13.** Pattern of surface current flow of Antenna III with Port 1 in excited mode at: (a) 20.8 GHz, (b) 22.4 GHz, (c) 24 GHz, and (d) 27.1 GHz.

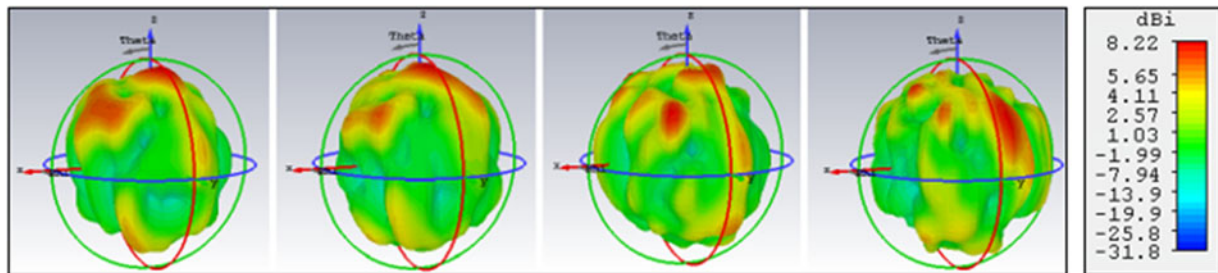


**Figure 14.** Far-field magnitude of Antenna III at: (a) 20.8 GHz, (b) 22.4 GHz, (c) 24 GHz, (d) 27.1 GHz.

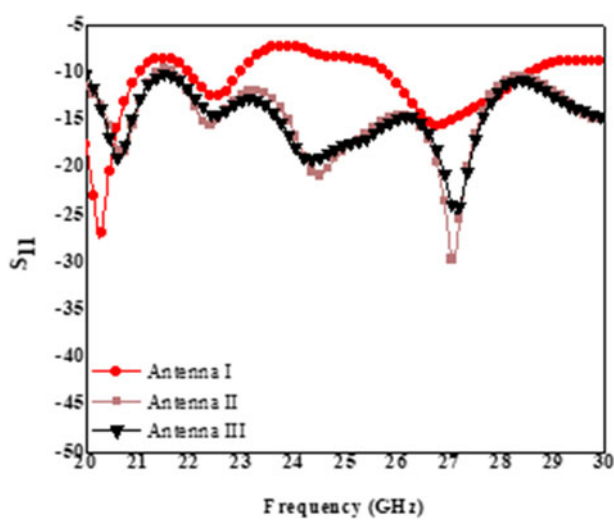


**Figure 15.**  $S_{11}$  vs. frequency response of Antenna I, II, and III.

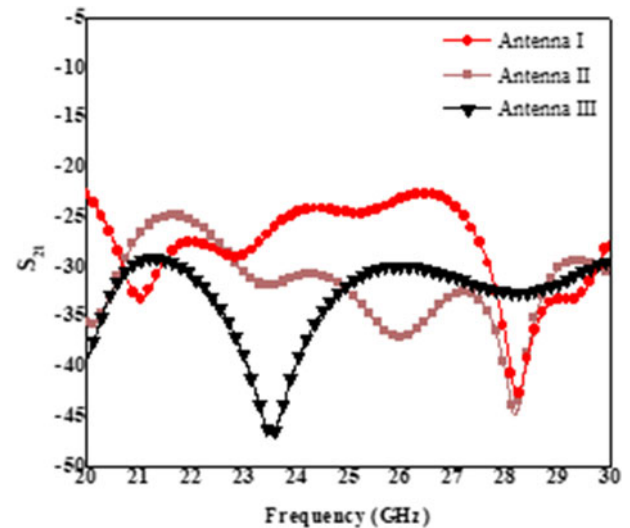


**Figure 16.**  $S_{22}$  vs. frequency response of Antenna I, II, and III.

As observed from Fig. 4, the antenna surface current in the ground plane is distributed evenly. Defected ground structures, as discussed earlier, have the ability to induce resonant modes in the frequency response of the antenna, which mainly occurs due to the disturbance in the antenna surface current flow. With the insertion of the rhombic slot, the surface current is disturbed, which can be observed from Fig. 9. The resonant modes so generated thereby come closer to one another, which in turn results in the increase in the overall bandwidth.

Researchers working on antennas have taken advantage of parasitic strips to improve isolation, as seen in [32]. Parasitic components are crucial in lowering the mutual coupling between antenna elements. Here, we have added a diagonal T-shaped stub to Antenna III to isolate the radiating components (Fig. 11).

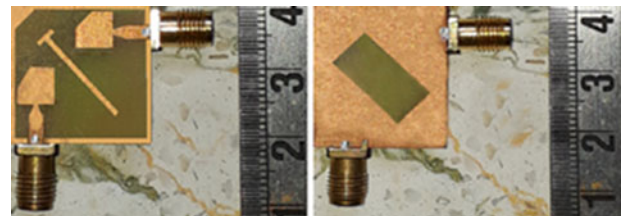


**Figure 17.** Fabricated prototype of Antenna III (front and rear views).

Figure 12 shows the S-parameter vs frequency response of Antenna III. The surface current flow pattern of Antenna III with Port 1 excited at 20.6 GHz, 22.2 GHz, 24.2 GHz, and 27.1 GHz is depicted in Fig. 13. Figure 14 shows Antenna III's field strength

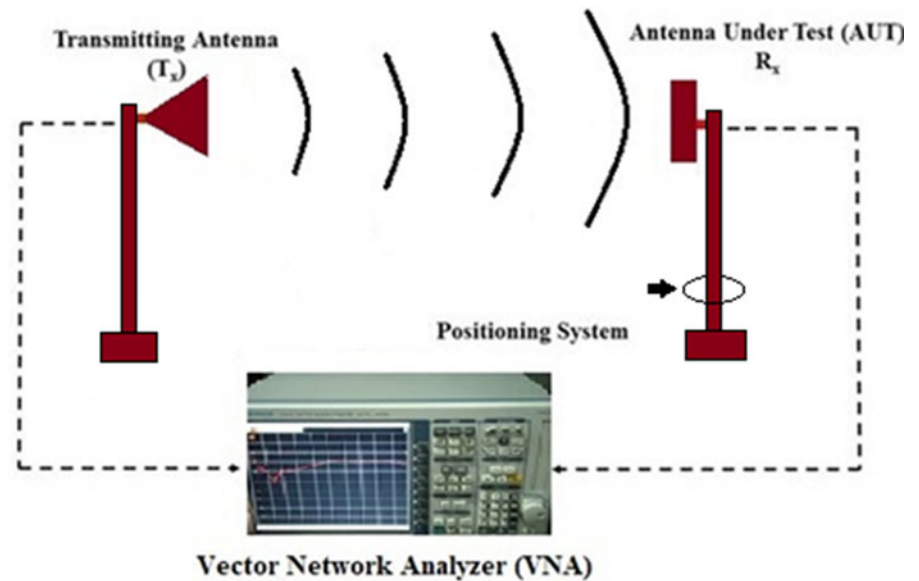


**Figure 18.** Schematic showing antenna operating and measurement process.

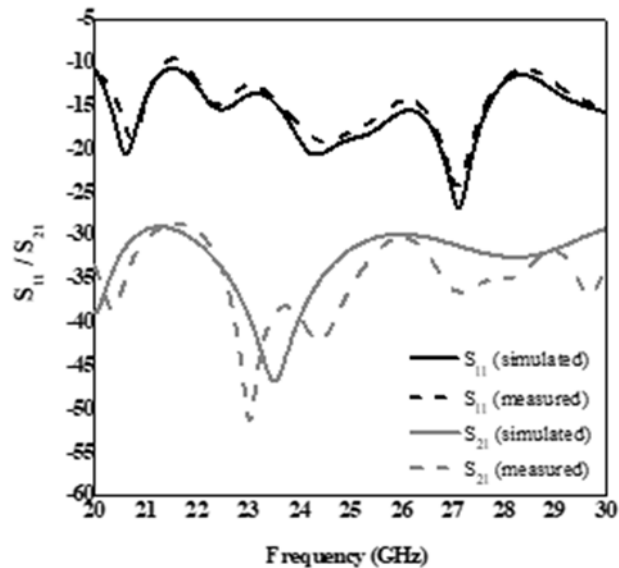


**Figure 19.** S-parameter vs. frequency response of Antenna III (simulated vs. measured).

at the same frequency points. As seen in Fig. 13, the presence of a parasitic stub prevents the flow of antenna current across ports, serving as a de-coupler and enhancing isolation. The antenna current is clearly seen to remain concentrated around the parasitic strip. Therefore, it is conceivable that the parasitic stub that is positioned between the two radiators is the cause of the deviation in the antenna current's path between ports.

The S-parameter vs. Freq. response charts for Antennas I, II, and III are shown in Figs. 15 and 16. Three distinct frequency bands (20–21.5 GHz), (22–23 GHz), and (26–29 GHz) have been acquired for Antenna I. In this instance, a maximum isolation level of –44 dB was attained. Antenna II displayed a broad bandwidth in simulation, spanning from 20.0 GHz to just over 28 GHz, despite the fact that the maximum isolation level (–45 dB) remained essentially same. Our suggested structure, Antenna III, on the other hand, produced a broad bandwidth of 20.0–28.1 GHz combined with an increased maximum isolation level of  $|S_{21}| = 47$  dB, which

is unquestionably a remarkable achievement in isolation improvement and reduced crosstalk as cross talk depends on the value of  $|S_{21}|$ . Higher the value of  $|S_{21}|$ , lesser will be the cross talk. The following are Antennas I, II, and III's varied dimensions:  $W = 20.0$ ,  $L = 20.0$ ,  $S1 = 4.0$ ,  $S2 = 16.0$ ,  $Sw = 7.0$ ,  $Sl = 16.0$ ,  $Fw = 2.0$ ,  $F1 = 4.25$ ,  $F2 = 2.25$ ,  $P1 = 4.0$ ,  $P2 = 6.5$ ,  $P3 = 6.5$ ,  $P4 = 3.0$ ,  $P5 = 4.75$ ,  $P6 = 3.25$ ,  $p = 0.75$ ,  $l = 4.0$ ,  $r = 0.75$  and  $s = 0.75$  mm.

### Antenna fabrication, measurement, and analysis

With expert assistance, the antenna prototype is created (Fig. 17). The walls are covered with urethane foam absorbers.

It may be mentioned here that as a reference antenna for measurement purposes, a standard gain pyramidal horn antenna (WR-22) made of Al-material with a nominal gain of 24.7 dBi has

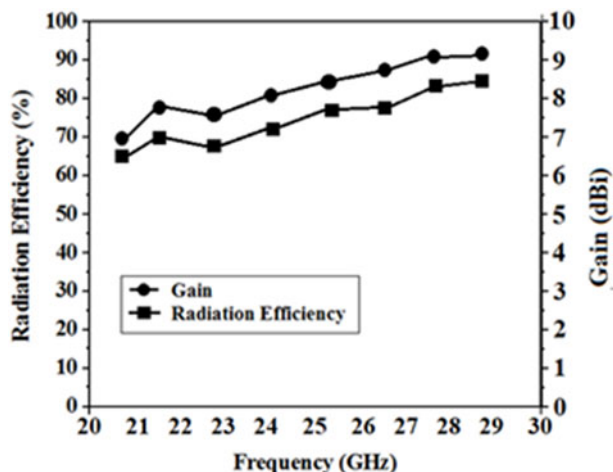


Figure 20. Rad. Eff. and gain plot of Antenna III (proposed antenna).

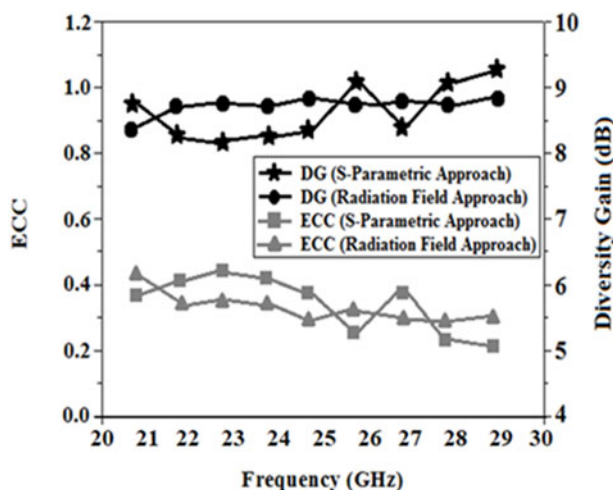


Figure 21. ECC and DG plot of Antenna III (proposed antenna).

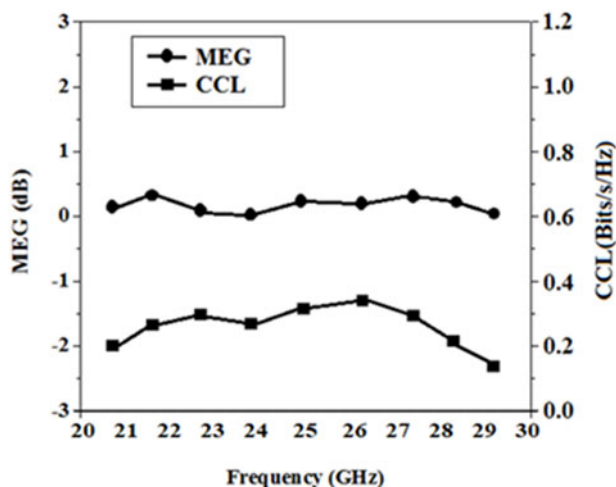


Figure 22. MEG and CCL plot of Antenna III (proposed antenna).

been employed. The Antenna under test is fixed to the positioning system, and N5-230A Vector Network Analyzer (VNA) was utilized to measure the antenna responses.

The entire operating and measurement process has been depicted in Fig. 18. The antenna under test (AUT) has been placed on the positioning system, which acts as the Receiver (Rx) antenna and the Transmitter (Tx) antenna used here is the horn antenna. Signal is radiated from the directional horn antenna and the same is received by the AUT. The signal responses are measured with the help of the VNA.

The S-parameter vs. Freq. response of the antenna is shown in Fig. 19. The values of the S-parameters are well matched for simulation and measurement as well. As seen in Fig. 19, the antenna produced a wide impedance bandwidth of 21.5–28.5 GHz and an enhanced isolation level of  $|S_{21}| = 25$  dB, which is unquestionably a significant advancement in isolation enhancement.

An antenna with a standard gain is kept on the turntable and calibrated in the bore-sight direction to measure the gain of the AUT. The antenna needs to be positioned correctly. The power level (relative) is now determined with the aid of VNA, which enables us to determine the relative gain of the antenna under inquiry [33]. Gain being a function of directivity, we may determine the gain/radiation pattern by altering the gain in different directions. Figure 20 shows the AUT’s gain and radiation efficiency.

Along the whole bandwidth, antenna gain varies from 7 to 9.3 dBi, while radiation efficiency varies from 65% to 85%.

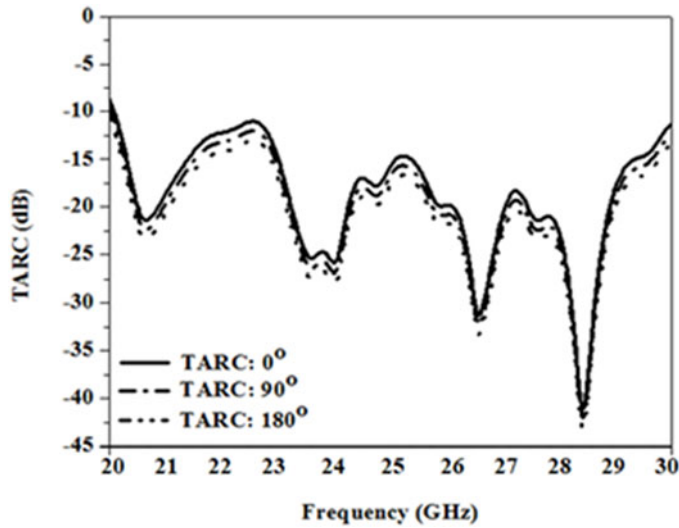


Figure 23. TARC plot of Antenna III (proposed antenna).

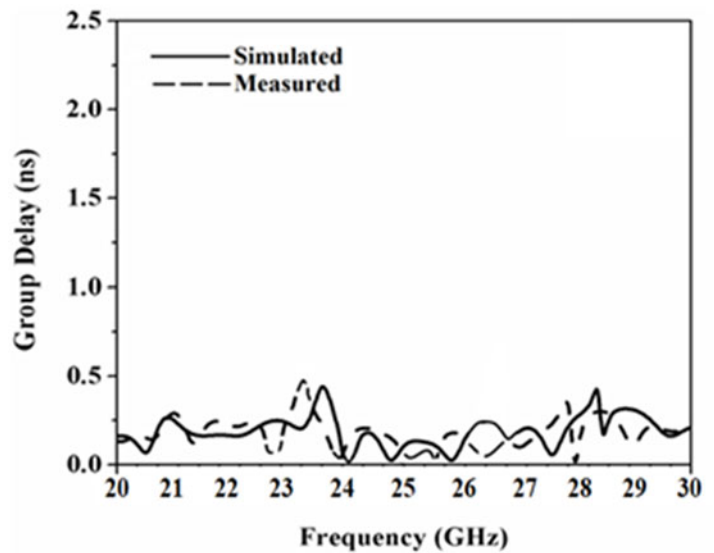


Figure 24. Group delay plot of Antenna III (sim. vs. mea.).

Envelope-Correlation-Coefficient or ECC, is crucial when examining a MIMO antenna’s diversity characteristic. It is a measure of the degree of independency of the antenna radiation patterns. Low value is an indication of higher isolation between multiple MIMO ports. Several methods can be used to calculate ECC. However, the “3D Radiation Pattern” approach is dependable and precise. Equation (1) may be used to compute the ECC for a MIMO antenna as,

$$\rho_e = \frac{\iint_{4\pi} |P_1(\phi, \varphi) P_2(\phi, \varphi)|^2 d\Omega}{\iint_{4\pi} |P_1(\phi, \varphi)|^2 d\Omega \iint_{4\pi} |P_2(\phi, \varphi)|^2 d\Omega} \quad (1)$$

where,  $P_i(\phi, \varphi) = P_{\theta}^i(\phi, \varphi)\vec{a}_{\theta} + P_{\phi}^i(\phi, \varphi)\vec{a}_{\phi}$  is the  $i$ th element’s radiation field [34]. Using Equation (1), the ECC for antennas may be determined using S-parameters [35] as follows:

$$\rho_e(p, q, R) = \frac{|C_{p,q}(R)|^2}{\prod_{k=(p,q)} [1 - C_{k,k}(R)]} \quad (2)$$

where  $C_{p,q}(R)$  is given as follows:

$$C_{p,q}(R) = \sum_{n=1}^R S_{p,n}^* S_{n,q}^2$$

ECC can also be used to determine diversity gain (DG) using Equation (3) as follows:

$$DG = 10\sqrt{1 - (\rho_e)^2} \quad (3)$$

Diversity techniques are used to reduce the fading effect. Diversity gain increases the concentration of probability density function (PDF) of the instantaneous value of signal-to-noise ratio (SNR), around its average value [36]. Low ECC and high DG are characteristics of an effective MIMO diversity antenna [37]. The suggested MIMO antenna’s ECC/DG is shown in Fig. 20 and was calculated using the radiation field approach and S-parametric techniques, respectively.

The proposed MIMO antenna, as seen in the image, has produced low ECC (0.45 dB) and high DG (9.3 dB), which are unquestionably encouraging numbers for strong antenna performance.

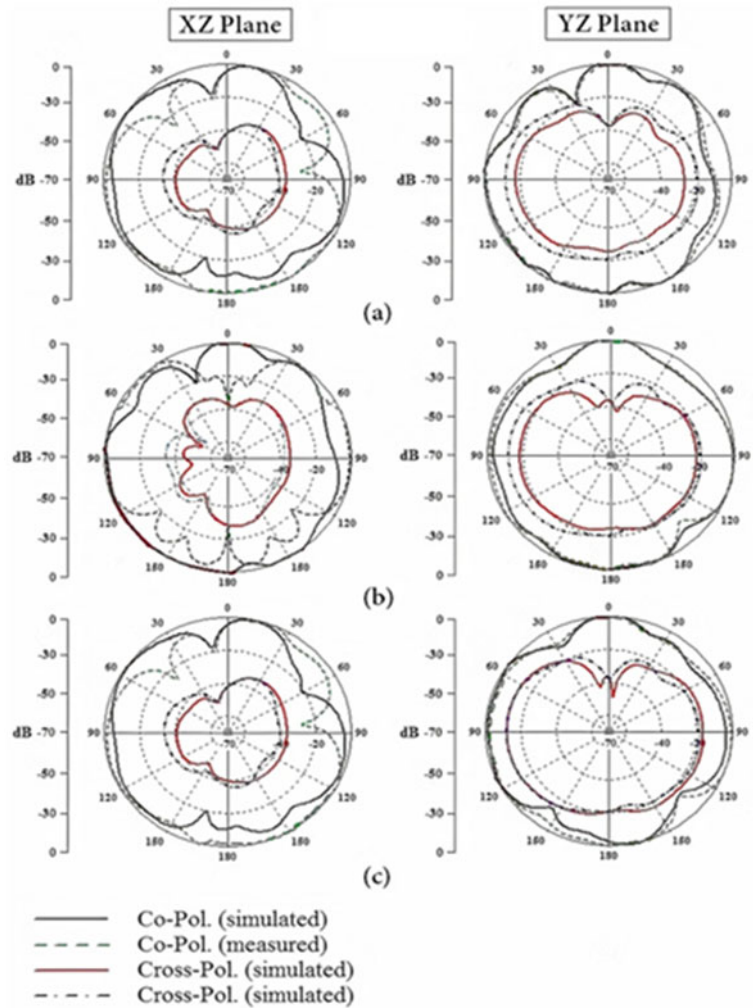


**Figure 25.** Radiation pattern of proposed antenna at YZ/XZ-plane: (a) 20.5 GHz, (b) 24.3 GHz, and (c) 27.2 GHz.

Channel Capacity is the maximum rate of transfer of information through a channel. The Channel Capacity Loss, or CCL is also a crucial parameter to be accounted for. For optimal performance with light channel capacity deterioration and good information transformation, it should be 0.4 Bits/s/Hz. Equation (4) can be used to calculate CCL as follows:

$$CCL = -\log_2 \det(\gamma^r) \tag{4}$$

where  $\gamma^r$  is the correlation matrix in this case [38]. Figure 21 shows the proposed MIMO antenna's CCL, which is around 0.37 Bits/s/Hz.

We can better comprehend the impact of fading by using Mean Effective Gain, or MEG. The ratio of the mean values of accepted to incident antenna power along a certain direction is known as MEG [39]. Equation (5) can be used to compute it as follows:

$$MEG_i = 0.5\nu_{p,rad} = 0.5(1 - \sum_{y=1}^N |S_{pq}|^2) \tag{5}$$

The MEG is less than 0.3 dB across the whole operational bandwidth, as can be seen in Fig. 22.

Total active reflection coefficient, often known as TARC, is a crucial metric to assess diversity characteristics, system performance, and impedance bandwidth in addition to the S-parameters. TARC for the suggested antenna can be calculated using equation (6) and the S-parameters as follows:

$$\Gamma = \frac{\sqrt{|S_{pp} + S_{pq}e^{j\varphi}|^2 + |S_{pq} + S_{qq}e^{j\varphi}|^2}}{\sqrt{2}} \tag{6}$$

Here,  $\varphi$  is the phase for activating the input port. Input and output ports' reflection coefficients are represented by  $S_{pp}$  and  $S_{qq}$ , respectively, and the isolation between the two ports is represented by  $S_{pq}/S_{qp}$  [39]. The TARC has been assessed in relation to a few excitation phase angles. Figure 23 shows the TARC curves for 0°, 90°, and 180°, which show good behavior over the whole operational spectrum.

A time domain response analysis is also required to determine the antenna group delay. Equation (7) yields

$$\text{the Group Delay, } \gamma_g = \frac{\Delta\alpha}{\Delta\beta} \tag{7}$$

where  $\Delta\alpha$  and  $\Delta\beta$  are the transmitted signal's phase deviation and frequency deviation [39], respectively. Group delay refers to

**Table 2.** A simplified error budget for the measurement of antenna gain

Standard horn antenna (SHA) gain measurement errors		Error in dB
1	Calibration accuracy of reference SHA	0.06
2	SHA return loss	0.04
3	Other measurement errors (linearity and circularity of receiver, probe response error, and reflectivity of chamber)	0.12
<b>Measurement errors of antenna under investigation (AUI)</b>		
1	Receiver circularity	0.03
2	Receiver linearity	0.01
3	RF system stability	0.05
4	Uniformity in response of probe	0.02
5	AUI return loss	0.04
6	Reflectivity of chamber	0.05
<b>Total error in gain</b>		<b>0.42</b>

the delay of the signal traveling through the test device as a function of frequency. It is an evaluation of the time required for the modulated signal to traverse the network [40, 41]. The suggested MIMO antennas in this design are spaced apart by 30 cm in both the face-to-face and side-by-side orientations to analyze the signal latency. Signal distortion happens as a result of group delay variation. Figure 24 shows the characteristic of antenna group delay. The fluctuation is only 0.5 ns, as can be seen in the image, which is an acceptable margin.

In this aspect, it may be mentioned that due to the emergence of independent platform communication system, there exists a probability of co-site interferences. Eminent researchers around the world have proposed several techniques for cancellation of this signal interference. Various adaptive co-site Interference Cancellation Systems (ACICS) have been proposed.

In this regard, effective techniques of broadband interference cancellation as in [42, 43] may be adopted to enhance the performance of the proposed MIMO antenna system. The interference cancellation bandwidth can be improved by delay matching, which has been validated after simulation followed by results of measurement.

In order to measure the radiation pattern across several planes (XZ/YZ), the AUT's orientation with respect to the reference horn antenna must be modified. Figure 25 shows the 2D-polar plot, which includes the simulated and measured antenna radiation patterns (including Cross-Pol. and Co-Pol.) for the XZ and YZ planes at frequencies of 20.5 GHz, 24.3 GHz, and 27.2 GHz, respectively. The pattern has few nulls and is slightly omnidirectional. Well-isolated co and cross polarization patterns are a positive indicator of the practical applicability of the antenna under test.

The proposed MIMO antenna uses multiple input and output streams efficiently for improved signal quality and diversity. By introducing multiple antennas in the transmitting and receiving ends, multipath fading reduction and channel capacity improvement can be achieved. For this purpose, the antenna should be compact in shape and size, portable, and uncorrelated to each other. Our proposed MIMO antenna structure satisfies all the aspects in this regard.

The main challenge faced during the entire process is taking into account of the various errors during the measurement of the

antenna gain. A simplified error budget has been prepared for the measurement of antenna gain, which is shown in Table 2.

## Conclusion

Here, a miniaturized, printed, isolation-enhanced  $2 \times 2$  MIMO antenna has been examined for various 5G communication uses. The dimensions of the antenna are  $20 \times 20 \times 1$  mm<sup>3</sup>. By sandwiching a parasitic element with the shape of "T" between two orthogonal radiators, an isolation margin of  $|S_{21}| \leq 29$  dB has been achieved. The final antenna configuration supports the 24/25 GHz and 27/28 GHz bands of the 5G spectrum, respectively, and exhibits a wide impedance bandwidth of 21.5–28.5 GHz. Compact dimensions, simplicity in design, wide bandwidth, and high isolation are its promising features. In addition, this antenna's planar design and incredibly small dimension makes it easy to be incorporated in wireless devices. Enhancement of MIMO modes will definitely add to the increased diversity feature, added gain and directivity. The choice of parasitic structures of different shapes and sizes is also an added scope here, which are the possible prospects of future investigation.

**Competing interests.** The author declares none.

## References

- Marcus M (2015) 5G and IMT for 2020 and beyond. *IEEE Wireless Communications* 22(4), 1–3.
- Zhang Y, Deng J, Li M, Sun D and Guo L (2019) A MIMO dielectric resonator antenna with improved isolation for 5G mm-wave applications. *IEEE Antennas and Wireless Propagation Letters* 18(4), 747–751.
- Sharawi M, Ikram M and Shamim A (2017) A two concentric slot loop based connected array MIMO antenna system for 4G/5G terminals. *IEEE Transactions on Antennas and Propagation* 65(12), 6679–6686.
- Chang L, Yu Y, Wei K and Wang H (2019) Polarization-orthogonal co-frequency dual antenna pair suitable for 5G MIMO smartphone with metallic bezels. *IEEE Transactions on Antennas and Propagation* 67(8), 5212–5220.
- Shoaib N, Shoaib S, Khattak R, Shoaib I, Chen X and Perwaiz A (2018) MIMO antennas for smart 5G devices. *IEEE Access* 6, 77014–77021.
- Alhalabi R and Rebeiz G (2008) High-efficiency angled-dipole antennas for millimeter-wave phased array applications. *IEEE Transactions on Antennas and Propagation* 56(10), 3136–3142.
- Deal W, Kaneda N, Sor J, Qian Y and Itoh T (2000) A new quasi-Yagi antenna for planar active antenna arrays. *IEEE Transactions on Microwave Theory & Techniques* 48(6), 910–918.
- Edward B and Rees D (1987) A broadband printed dipole with integrated balun. *Microwave Journal* 30(5), 339–344.
- Chattha H (2019) Compact high isolation wideband 4G and 5G multi-input multioutput antenna system for handheld and internet of things applications. *International Journal of RF and Microwave Computer-Aided Engineering* 29, e21710.
- Komandla M, Mishra G and Sharma S (2017) Investigations on dual slant polarized cavity-backed massive MIMO antenna with beamforming. *IEEE Transactions on Antennas and Propagation* 65(12), 6794–6799.
- Ojaroudiparchin N, Shen M and Pedersen G (2018) Small-size tapered slot antenna (TSA) design for use in 5G phased array applications. *The Applied Computational Electromagnetics Society Journal* 32, 193–202.
- Zhang S, Chen X, Syrytsin I and Pedersen G (2017) A planar switchable 3-D-coverage phased array antenna and its user effects for 28-GHz mobile terminal applications. *IEEE Transactions on Antennas and Propagation* 65(12), 6413–6421.
- Nor N, Jamaluddin M, Kamarudin M and Khalily M (2016) Rectangular dielectric resonator antenna array for 28GHz applications. *Progress in Electromagnetics Research C* 63, 53–61.

14. Ershadi S, Keshkar A, Abdelrahman A and Xin H (2017) Wideband high gain antenna subarray for 5G applications. *Progress In Electromagnetics Research C* **78**, 33–46.
15. Jilani S and Alomainy A (2018) Millimetre-wave T-shaped MIMO antenna with defected ground structures for 5G cellular networks. *IET Microwaves, Antennas & Propagation* **12**(5), 672–677.
16. Abbas E, Ikram M, Mobashsher A and Abbosh A (2019) MIMO antenna system for multi-band millimeter-wave 5G and wideband 4G mobile communications. *IEEE Access* **7**, 181916–181923.
17. Kumar DR, Sangeetha T, Sujanth Narayan K, Venkat Babu G, Prithvirajan V and Manikandan M (2023) A miniaturized CPW-fed CSRR-loaded quad-port MIMO antenna for 5.5/6.5 GHz wireless applications. *International Journal of Microwave and Wireless Technologies*, 1–10.
18. Bhattacharya A, Roy B, Chowdhury SK and Bhattacharjee AK (2022) An isolation enhanced, printed, low-profile UWB-MIMO antenna with unique dual band-notching features for WLAN and WiMAX. *IETE Journal of Research* **68**(1), 496–503.
19. Kaur H, Singh H and Upadhyay R (2023) Design and analysis of planar four-port UWB-MIMO antenna with band-rejection capability. *International Journal of Microwave and Wireless Technologies*, 1–13.
20. Talha M, Babu M and Aldhaheri R (2016) Design of a compact MIMO antenna system with reduced mutual coupling. *International Journal of Microwave and Wireless Technologies* **8**, 117–124.
21. Bang J and Choi J (2018) A SAR reduced mm-wave beam-steerable array antenna with dual-mode operation for fully metal-covered 5G cellular handsets. *IEEE Antennas and Wireless Propagation Letters* **17**, 1118–1122.
22. Das G, Sharma A, Gangwar R and Sharawi M (2018) Compact back-to-back DRA-based four-port MIMO antenna system with bi-directional diversity. *Electronics Letters* **54**, 884–886.
23. Kumar A and Rosaline I (2021) Hybrid half-mode SIW cavity-backed diplex antenna for on-body transceiver applications. *Applied Physics A* **127**(11), 1–7.
24. Chaturvedi D and Raghavan S (2019) Dual-band, dual-fed self-diplexing antenna. In *2019 13th European Conference on Antennas and Propagation (EuCAP)*, 31 March 2019, 1–5.
25. Rosaline I, Kumar A, Upadhyay P and Murshed A (2022) Four element MIMO antenna systems with decoupling lines for high-speed 5G wireless data communication. *International Journal of Antennas and Propagation* **2022**, 1–13.
26. Gong X, Tong L, Tian Y and Gao B (2015) Design of a microstrip fed spade shape planar monopole antenna for UWB applications. In *2015 IEEE 6th International Symposium on Microwave, Antenna-, Propagation, and EMC Technologies (MAPE)*, Shanghai, 227–230.
27. Roy B, Bhattacharya A, Bhattacharjee AK and Chowdhury SK (2015) A novel wideband spade shaped monopole antenna with ring geometry for wireless applications. In *2015 International Conference on Electronic Design, Computer Networks & Automated Verification (EDCAV)*, Shillong, India, 110–113.
28. Di W and Li J-S (2013) Compact spade-shaped antenna with a band-notched characteristic for UWB application. In *2013 5th IEEE International Symposium on Microwave, Antenna-, Propagation and EMC Technologies for Wireless Communications*, Chengdu, China, 429–431.
29. Cho Y, Kim K, Choi D, Lee S and Park S (2006) A UWB planar monopole antenna with 5.0 GHz band-rejection filter and the time-domain characteristics. *IEEE Transactions on Antennas and Propagation* **54**, 1453–1460.
30. Jan J and Kao J (2007) Novel wideband rhombus like slot antenna with an offset microstrip fed line. *IEEE Antennas and Wireless Propagation Letters* **6**, 249–251.
31. Rehman S, Sheta A and Alkanhal M (2011) Compact bandpass filters with bandwidth control using DGS. *The Applied Computational Electromagnetics Society Journal* **26**, 624–630.
32. Ding K, Gao C, Qu D and Yin Q (2017) Compact broadband MIMO antenna with parasitic strip. *IEEE Antennas and Wireless Propagation Letters* **16**, 2349–2353.
33. Balanis C (1997) *Antenna Theory Analysis and Design*, 2nd edn. New York: John Wiley & Sons, Inc.
34. Liu Y, Yang X, Jia Y and Guo YJ (2019) A low correlation and mutual coupling MIMO antenna. *IEEE Access* **7**, 127384–127392.
35. Hallbjorner P (2005) The significance of radiation efficiencies when using S-parameters to calculate the received signal correlation from two antennas. *IEEE Antennas and Wireless Propagation Letters* **4**(1), 97–99.
36. Jing X, Lin Y, Liang B and Shen J (2022) Chapter 15 – 5G Ultra-reliable and low-latency communication: PHY layer. In Jia Shen, Zhongda Du, Zhi Zhang, Ning Yang, Hai Tang (eds), *5G NR and Enhancements*. Elsevier, 687–739.
37. Biswas A, Pattanayak S and Chakraborty U (2020) Evaluation of dielectric properties of colored resin plastic button to design a small MIMO antenna. In *IEEE Transactions on Instrumentation and Measurement*.
38. Nej S, Ghosh A, Ahmad S, Kumar J, Ghaffar A and Hussein MI (2022) Design and characterization of 10-elements MIMO antenna with improved isolation and radiation characteristics for mm-Wave 5G applications. *IEEE Access* **10**, 125086–125101.
39. Chae S, Kawk W, Park S and Lee K (2006) Analysis of mutual coupling in MIMO antenna array by TARC calculation. In *2006 Asia-Pacific Microwave Conference*, Yokohama, Japan, 2090–2093.
40. Sharma P, Tiwari R, Singh P and Kanaujia BK (2022) Dual-band trident shaped MIMO antenna with novel ground plane for 5G applications. *AEU – International Journal of Electronics and Communications* **155**, 154364.
41. Mahto SK, Singh AK, Sinha R, Alibakhshikenari M, Khan S and Pau G (2023) High isolated four element MIMO antenna for ISM/LTE/5G (Sub-6GHz) Applications. *IEEE Access* **11**, 82946–82959.
42. Jiang Y and Li X (2022) Broadband cancellation method in an adaptive co-site interference cancellation system. *International Journal of Electronics* **109**(5), 854–874.
43. Jiang Y, Liu S, Li M, Zhao N and Wu M (2022) A new adaptive co-site broadband interference cancellation method with auxiliary channel. *Digital Communications and Networks*.



Ankan Bhattacharya completed his PhD at the National Institute of Technology, Durgapur, India. He is the author of several research papers that have been published in many reputed journals and conferences at the national and international levels. He is a life member of the Forum of Scientists, Engineers & Technologists, a member of the Institution of Engineers India, a member of the International Association of Engineers, and

a member of the Internet Society (ISOC). His areas of research are antenna engineering, computational electromagnetics, electronic circuits and systems, signal processing, microwave devices, and wireless communication technologies. He is an editor and reviewer of many national and international journals of repute. He has organized and participated in many national and international conferences, seminars, and workshops. He has been active in delivering invited talks and has also been a part of many national and international conferences in the capacity of coordinator, session chair, technical committee member, etc. Presently he is associated with Hooghly Engineering & Technology College, Hooghly, West Bengal, India as an Associate Professor and Head of the Electronics and Communications Engineering Department.